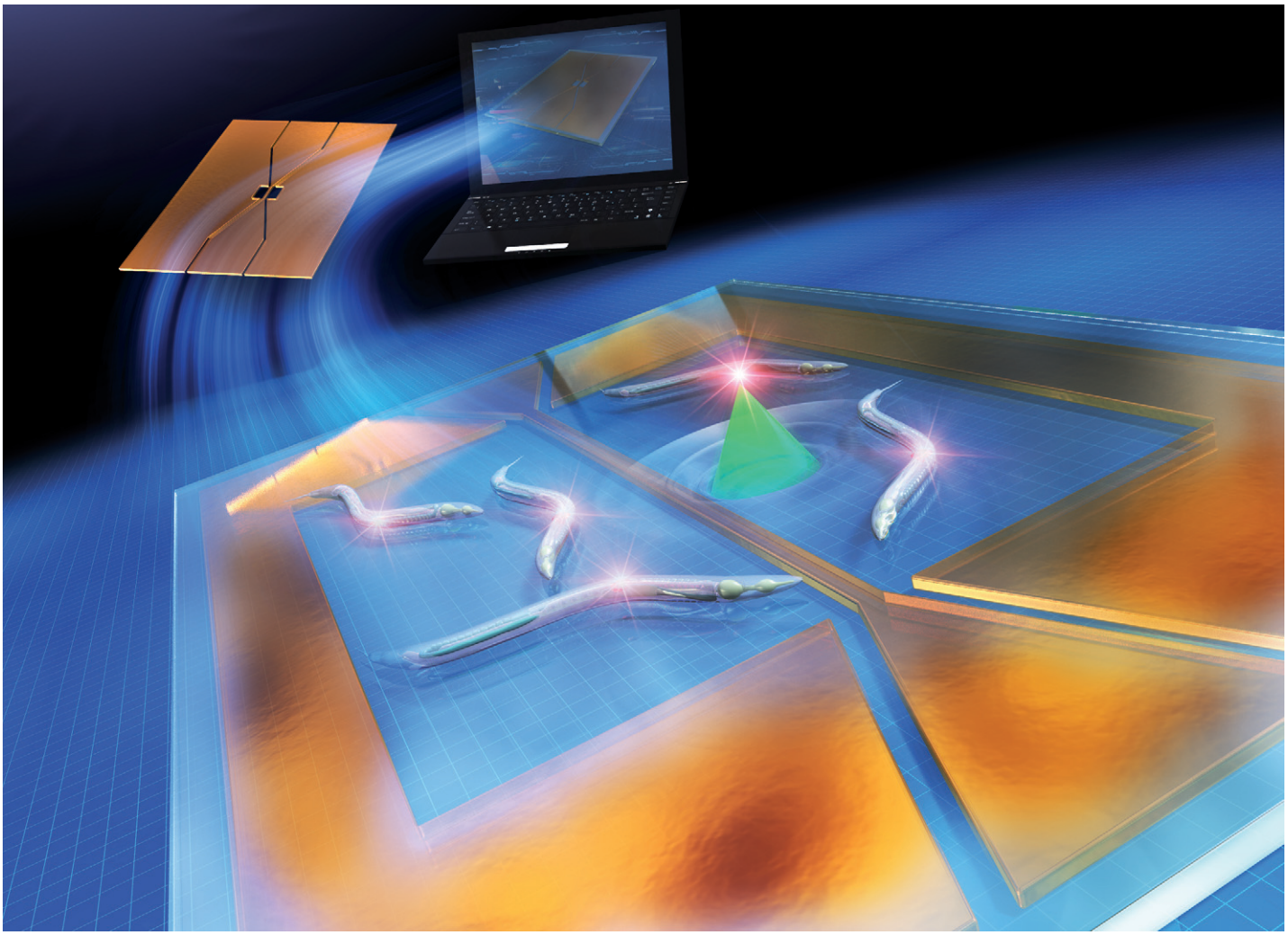

Showcasing research from Professor Masazumi Fujiwara's laboratory, Department of Chemistry, Graduate School of Natural Science and Technology, Okayama University, Japan.

Glass-patternable notch-shaped microwave architecture for on-chip spin detection in biological samples

A novel microwave architecture on a glass chip realizes large-area and predictable electron spin detection of fluorescent nanodiamonds in various bioassay chips, which will provide a scalable platform for quantum-sensor-based bioassay using nanodiamonds.

As featured in:

See Keisuke Oshimi, Masazumi Fujiwara *et al.*, *Lab Chip*, 2022, 22, 2519.

ROYAL SOCIETY OF CHEMISTRY

rsc.li/loc

Registered charity number: 207890

Lab on a Chip

PAPER

View Article Online
View Journal | View Issue

Cite this: *Lab Chip*, 2022, **22**, 2519

Glass-patternable notch-shaped microwave architecture for on-chip spin detection in biological samples†

Keisuke Oshimi,[ab] Yushi Nishimura,[bc] Tsutomu Matsubara,[d] Masuaki Tanaka,[e] Eiji Shikoh,[e] Li Zhao,[f] Yajuan Zou,[ag] Naoki Komatsu,[g] Yuta Ikado,[a] Yuka Takezawa,[h] Eriko Kage-Nakadai,[h] Yumi Izutsu,[i] Katsutoshi Yoshizato,[j] Saho Morita,[k] Masato Tokunaga,[k] Hiroshi Yukawa,[klc] Yoshinobu Baba,[klc] Yoshio Teki[b] and Masazumi Fujiwara*[ab]

Received 3rd February 2022,
Accepted 26th April 2022

DOI: 10.1039/d2lc00112h

rsc.li/loc

We report a notch-shaped coplanar microwave waveguide antenna on a glass plate designed for on-chip detection of optically detected magnetic resonance (ODMR) of fluorescent nanodiamonds (NDs). A lithographically patterned thin wire at the center of the notch area in the coplanar waveguide realizes a millimeter-scale ODMR detection area (1.5 × 2.0 mm^2) and gigahertz-broadband characteristics with low reflection (~8%). The ODMR signal intensity in the detection area is quantitatively predictable by numerical simulation. Using this chip device, we demonstrate a uniform ODMR signal intensity over the detection area for cells, tissue, and worms. The present demonstration of a chip-based microwave architecture will enable scalable chip integration of ODMR-based quantum sensing technology into various bioassay platforms.

1 Introduction

The miniaturization and compactification of analytical systems into chip devices are crucial for achieving efficient high-throughput and highly sensitive bioassays with significantly reduced sample numbers and volumes.[1–3] Implementing small, sensitive, and multimodal sensors into a detection area is key for realizing miniaturized assay devices. Ultrasensitive multimodal nanometer-sized quantum sensors based on fluorescent nanodiamonds (NDs) have been applied to various biological systems, including biomolecules,[4–9] cells,[10–14] and small organisms.[15–17] Nanodiamonds have a low cytotoxicity,[18–20] and their surfaces can be functionalized for biological targeting and labeling.[21–23] In most workflows, they first bind to target molecules or cells to produce labeled samples that are subsequently introduced into the detection area for multimodal quantum sensing. The sensing multimodality of NDs results from the dependence of electron-spin-resonance frequencies of nitrogen vacancy (NV) centers on the magnetic field,[24–26] electric field,[27–29] and temperature.[30–32] It is detected through the modulation of fluorescence intensity by microwave excitation and referred to as optically detected magnetic resonance (ODMR). As ODMR uses fluorescence detection and microwave excitation, scaling down an ODMR-based bioassay into a chip device relies on the miniaturization of both these technologies. By exploiting the suitability of optical methods at the submillimeter scale, several fluorescence-detection techniques and measurement systems

[a] *Department of Chemistry, Graduate School of Natural Science and Technology, Okayama University, Okayama 700-8530, Japan. E-mail: masazumi@okayama-u.ac.jp*
[b] *Department of Chemistry, Graduate School of Science, Osaka City University, Osaka 558-8585, Japan*
[c] *Institute for Quantum Life Science, Quantum Life and Medical Science Directorate, National Institutes for Quantum Science and Technology, Chiba 263-8555, Japan*
[d] *Department of Anatomy and Regenerative Biology, Graduate School of Medicine, Osaka City University, Osaka 545-8585, Japan*
[e] *Department of Electrical and Information Engineering, Graduate School of Engineering, Osaka City University, Osaka 558-8585, Japan*
[f] *State Key Laboratory of Radiation Medicine and Protection, School for Radiological and Interdisciplinary Sciences (RAD-X) and Collaborative Innovation Center of Radiation Medicine of Jiangsu Higher Education Institutions, Soochow University, Suzhou 215123, P. R. China*
[g] *Graduate School of Human and Environmental Studies, Kyoto University, Kyoto 606-8501, Japan*
[h] *Department of Human Life Science, Graduate School of Food and Human Life Science, Osaka City University, Osaka 558-8585, Japan*
[i] *Department of Biology, Faculty of Science, Niigata University, Niigata 950-2181, Japan*
[j] *Synthetic biology laboratory, Graduate school of medicine, Osaka City University, Osaka 545-8585, Japan*
[k] *Department of Biomolecular Engineering, Graduate School of Engineering, Nagoya University, Nagoya 464-8603, Japan*
[l] *Institute of Nano-Life-Systems, Institutes of Innovation for Future Society, Nagoya University, Nagoya 464-8603, Japan*

† Electronic supplementary information (ESI) available. See DOI: https://doi.org/10.1039/d2lc00112h

have been used in chip devices,[33–35] which are readily utilized for ODMR. For microwave manipulation, several architectures have been reported for on-chip thermal control, analyte sensing, and spin detection.[36–39] However, the miniaturization of microwave excitation circuits into ODMR chip devices has been challenging, owing to difficulties in providing broad-band and large-area microwave excitation in a chip-integrable configuration, while having high-efficiency fluorescence photon collection in aqueous environments.

Several types of microwave circuitry have been used as emission antennas for ODMR measurements, including thin wires,[7,40] coplanar waveguides,[41,42] coils,[43,44] and omega-shaped patterns.[8,45,46] Thin wires or coplanar waveguides produce a strong excitation intensity around the transmission wires or gaps; hence, the ODMR detection area is limited to ~100 μm. Coils can provide a more spatially uniform excitation area, but their excitation intensity is limited. Further, the observed ODMR signal intensity substantially depends on the coupling losses and sample-antenna distances that vary experiment by experiment, hindering the scalable engineering of ODMR chip devices. Omega-shaped patterns have recently been reported as an efficient and designable platform for microwave delivery, enabling paper-based lateral-flow assays with portable microwave devices.[8] However, their frequency bandwidth is approximately 70 MHz, and the 5 cm antenna size cannot be further scaled down owing to the cavity resonance effect, which limits ODMR applications that require a broad bandwidth of up to 400 MHz, such as vector magnetometry[47–50] and nanoscale NMR spectroscopy.[51–53] None of these circuity patterns fully satisfy the requirements of a millimeter-scale detection area, gigahertz bandwidth, and scalability for multiple detection areas within a small volume, all of which are necessary for the chip integration of diamond ODMR technology.

This study proposes a notch-shaped coplanar antenna on a glass plate that achieves a millimeter-scale ODMR detection area and broadband low-reflection microwave characteristics. A lithographically patterned thin wire at the center of the notch area in the coplanar waveguide generates spatially uniform and broadband excitation pattern of microwave magnetic field. We demonstrate ODMR measurements over a 1.5 × 2.0 mm^2 chip area, and even quantitatively predicting the ODMR signal intensity in the antenna detection area. By integrating this antenna within multiple bioassay platforms (including dishes and plates), uniform ODMR detection is observed for NDs labeled in cultured cells, tissue, and nematode worms. The scalability of the present microwave architecture facilitates the integration of ODMR detection areas within large-scale multi-well plates. Thus, we expect the present concept of a notch-shaped coplanar antenna to greatly extend the applicability of diamond quantum sensing to chip-based bioassays.

2 Methods

2.1 Numerical modeling of chip devices

The chip device was numerically designed using the COMSOL finite element method (FEM) software package with an RF module. It consists of an antenna-patterned coverslip with plastic supports. Numerical simulations were performed for the coverslip, neglecting the effect of the plastic supports on the overall microwave characteristics (as confirmed in Fig. S1†). We assumed a coverslip thickness of 0.17 mm and an infinitely thin gold-patterned layer on one side. The borosilicate glass coverslip was simulated with a relative permittivity ε = 4.6, relative permeability μ = 1.0, and electrical conductivity σ = 0.0 S m^{-1}. The thin gold layer was considered as a perfect electric conductor (PEC). A 70 mm radius sphere, filled with air (ε = 1.0, μ = 1.0, σ = 0.0 S m^{-1}), surrounded the coverslip, and a perfectly matched layer with an absorption constant of 10^{-6} was set at the sphere boundary. The mesh was created using the software's physics-controlled mode. The mesh size was chosen to ensure the convergence of the simulation results (Fig. S2†).

2.2 Device fabrication

Borosilicate glass coverslips Matsunami, with dimensions of 22 × 22 mm^2 for Part No. C022221 and 30 × 40 cm^2 sizes for Part No. C030401, and a thickness of 0.13–0.17 mm were cleaned with an alkali detergent. Photomasks were fabricated and used for transferring the patterns to coverslips using standard photolithography, as follows. Gold was deposited on coverslips with a 100 nm thickness (chromium buffer layer of ~3 nm). A photoresist (MicroChemicals, AZ 1500) was spin-coated at 4000–4500 rpm and baked at 95 °C for 90 s. The gold-coated coverslips were then exposed to a mercury lamp for 18 s, and the resist was removed. Gold and chromium were removed using appropriate etchants (AURUM-302 for gold and Cr-201 for chromium, both from Kanto Chemical Co.). The coverslips were washed with acetone to remove residual photoresist and bonded with dishes or multiwell plates using polydimethylsiloxane (75 °C, 1 h). Most of the experiments described below used 35 mm plastic dishes with an identical central hole diameter of 14 mm for ease of handling.

2.3 Scattering parameter characterization

We characterized the transmission and reflection of the antenna in the microwave frequency range by measuring the scattering parameters (*S*-parameters). Of the four two-port *S*-parameters, S_{11} and S_{21} were determined in both the simulation and the experiments. In this study, we expressed the reflection and transmission properties of the devices in dB units as:

$$S_{11} = 10\log_{10}\frac{P_{\text{reflected}}}{P_{\text{incident}}} \quad (1)$$

$$S_{21} = 10\log_{10}\frac{P_{\text{transmission}}}{P_{\text{incident}}}$$

where P_{incident}, $P_{\text{reflected}}$, and $P_{\text{transmission}}$ denote the incident, reflected, and transmitted powers, respectively.[54] These parameters were determined using COMSOL in the simulation

and experimentally using a network analyzer (MS46122B, Anritsu).

2.4 ND spin-coating on the coverslips

To perform ODMR measurements on NDs directly deposited onto the coverslips, we spin-coated 20 μL of a commercially available ND suspension (Adámas Nanotechnologies, ND-NV-100 nm-Hi) onto the antenna-patterned coverslips at 2000 rpm for approximately 30 s. The NDs were spin-coated on either the Au–Cr layer side or the reverse glass side to determine the microwave magnetic field magnitude $|\boldsymbol{B}|$.

2.5 ND labeling of biological samples

For the cell experiments, HeLa cells and adipose tissue-derived stem cells (ASCs) were cultivated in dish-style chip devices. HeLa cells and ASCs were labeled with NDs, as previously described.[55,56] The NDs with concentrations of 10 μg mL^{-1} and 20 μg mL^{-1} (Adámas Nanotechnologies, ND-NV-100 nm-Hi) were added to the culture media of HeLa cells and ASCs, respectively. The cells were incubated at 37 °C, 5% CO_2 for 24 h, washed three times with phosphate-buffered saline, and immersed in the respective culture media.

Tadpoles were anesthetized using MS222,[57,58] and polyglycerol-grafted NDs (PG-NDs)[23,59] were introduced into the tail by intramuscular injection using a syringe. The tail tips were isolated and placed in the measurement area of the chip device.

For the worm experiments, young adult *Caenorhabditis elegans* (*C. elegans*) were used. The wild-type *C. elegans* strain Bristol N2 was obtained from the Caenorhabditis Genetics Center (Minneapolis, MN, USA) and maintained following the standard protocol.[60] Next, PG-NDs were microinjected into the gonads as previously described.[17] The ND-labeled *C. elegans* were placed on the measurement area of the chip devices with agar pads.

2.6 ODMR experiments

The ODMR was measured using our home-built confocal fluorescence microscope equipped with a microwave excitation system.[17,56,61,62] Microwaves were generated by a signal generator (Rohde & Schwarz, SMB100A) and sent to a radiofrequency switch (Mini-circuit, ZYSWA-2-50DRS and General Microwave, F9160) triggered by a bit-pattern generator (SpinCore, PBESR-PRO-300). The signal was then amplified using an amplifier (Mini-circuit, ZHL-16W-43+). The fluorescence signal was detected by a single photon counting module (Excelitas, SPCM-AQRH-14) using conventional confocal microscopy.[55,63] The ODMR signal was measured in both the continuous wave (CW) and pulsed modes. In the CW mode, the microwave excitation was gated ON and OFF to suppress noise. The CW ODMR measurements were performed on the NDs placed directly on coverslips and for the NDs in biological samples, as described above. In the pulsed mode, Rabi measurements were performed to determine the duration of the π-pulse for NV electron spins. The pulsed ODMR measurements were performed only on the NDs on the coverslips. In addition, in the pulsed measurements, external magnetic fields were applied using neodymium magnets to lift the degeneracy of the magnetic sublevels to allow clear Rabi-nutation detection.

3 Results

3.1 Numerical modeling of the chip devices

Fig. 1(a) shows the fabrication workflow for our chip devices, from photolithography to coverslip bonding to various bioassay platforms (35 mm dishes and three-well plates in this figure). We first designed a microwave antenna pattern on a coverslip by numerical simulation and transferred the designed pattern onto coverslips using standard photolithography. The fabricated antenna-patterned coverslips were then bonded with conventional bioassay platforms such as dishes, multi-well plates, and microscope slides designed for efficient handling. Finally, these chip devices were docked[17] on our custom printed circuit board (PCB) comprising a coplanar waveguide and connectors (see Fig. 1(b) and (c)). We fabricated the chip devices in a dish, multi-well plate, and microscope slide. We primarily used the dish-style devices in the following experiments because of their ease of handling.

We simulated microwave antenna characteristics using FEM to optimize the structures for microwave irradiation. The basic design of the proposed antenna is illustrated in Fig. 2(a) and (b). The device is a notch-shaped coplanar waveguide with a tapered transmission line. The peripheral gold layer coating serves to adequately ground the device to the PCB. The multiple geometry parameters were determined for efficient input and large-area microwave irradiation at 2.87 GHz. The borosilicate glass coverslips had a typical thickness of t_g = 0.17 mm, and a thin gold layer was deposited with a thickness of $t_a \sim 100$ nm (with a chromium buffer layer of a few nanometers). The simulation assumed a coverslip relative permittivity ε = 4.6 and an infinitesimally thin PEC layer for the thin gold film (see Methods for more information on the material parameters). With these experimental constraints, we determined the width of the transmission wire at the coverslip edges to be w_1 = 1.5 mm and the gap width between the transmission wire and lateral ground region as g = 0.1 mm, giving a 50 Ω impedance to match that of the coaxial cables. The notch shape is characterized by its width a and height b and by the width of the central thin transmission wire w_2. For the purpose of ODMR detection in biological samples, we find that a = 1.5 mm, b = 2.0 mm, and w_2 = 50 μm is a good trade-off between the area size and magnetic field intensity, as described below. The tapered structures connecting the coplanar waveguides and the notch area act as an impedance transformer that raises the 50 Ω impedance to the higher impedance of the central thin transmission wire (approximately 300 Ω).[64,65]

With this geometry, we calculated the spatial distribution of the $|\boldsymbol{B}|$ and S-parameter spectra of the coverslip antenna, as shown in Fig. 2(c) and (d). In the spatial pattern of $|\boldsymbol{B}|$ at 2.87 GHz, microwaves emitted from the transmission wire reach the ground plane of the notch area and a uniform intensity $|\boldsymbol{B}|$ =

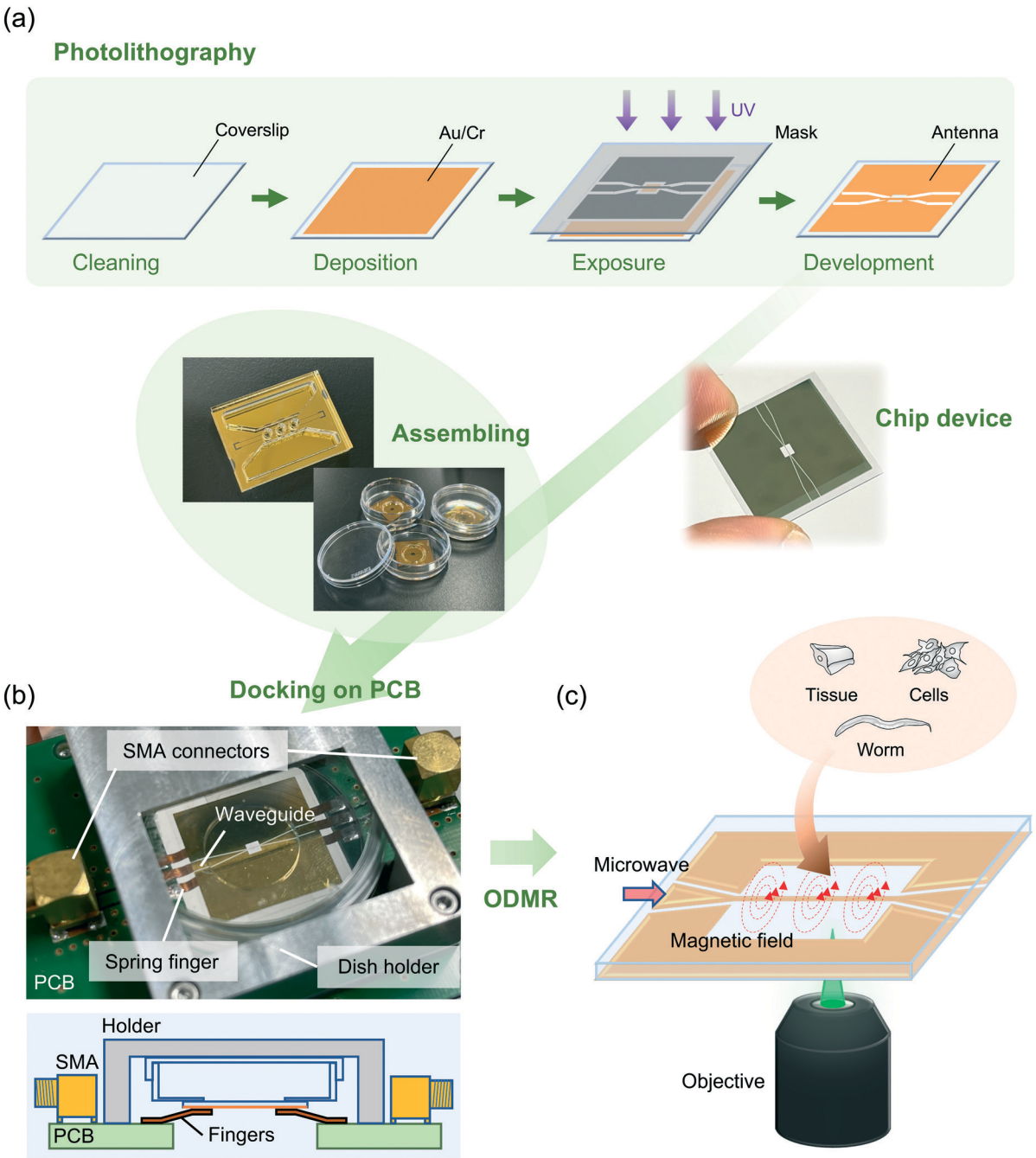

Fig. 1 (a) Chip fabrication scheme, including photolithography and bonding to bioassay platforms (35 mm dishes and three-well plates). (b) Photograph of a dish-style chip device docked to a PCB circuit board (top), and a schematic side-view diagram of the board and copper spring fingers (bottom). (c) Schematic spatial arrangement of biological samples relative to the waveguide pattern and microscope objective.

0.3 G is produced over 1.5 mm along the x axis (see values in Fig. 4(e)). This enables the observation of ODMR over the entire area, as described in sec. 2. A strong magnetic field of up to $|\boldsymbol{B}|$ = 6 G was also formed around the thin wire. While maintaining a large area of microwave excitation, the antenna conserves the broadband characteristics typical of coplanar waveguides, as shown in the S_{11} and S_{21} spectra (Fig. 2(d)).

We found that this spatially uniform and broadband excitation pattern originated from the thin wire that remained at the center of the notch area. Fig. 2(e) and (f) show, respectively, the simulated spatial pattern of $|\boldsymbol{B}|$ at 2.87 GHz and the S-parameter spectra when the thin wire is removed. In the absence of the thin wire, $|\boldsymbol{B}|$ nearly vanishes in the notch area, and S_{11} shows near-perfect reflection (S_{11} = 0), indicating that no microwaves enter the notch area. These results clearly demonstrate the effectiveness of the thin wire structure in the notch area for simultaneously realizing a strong magnetic field intensity, broadband frequency width, and large-area excitation.

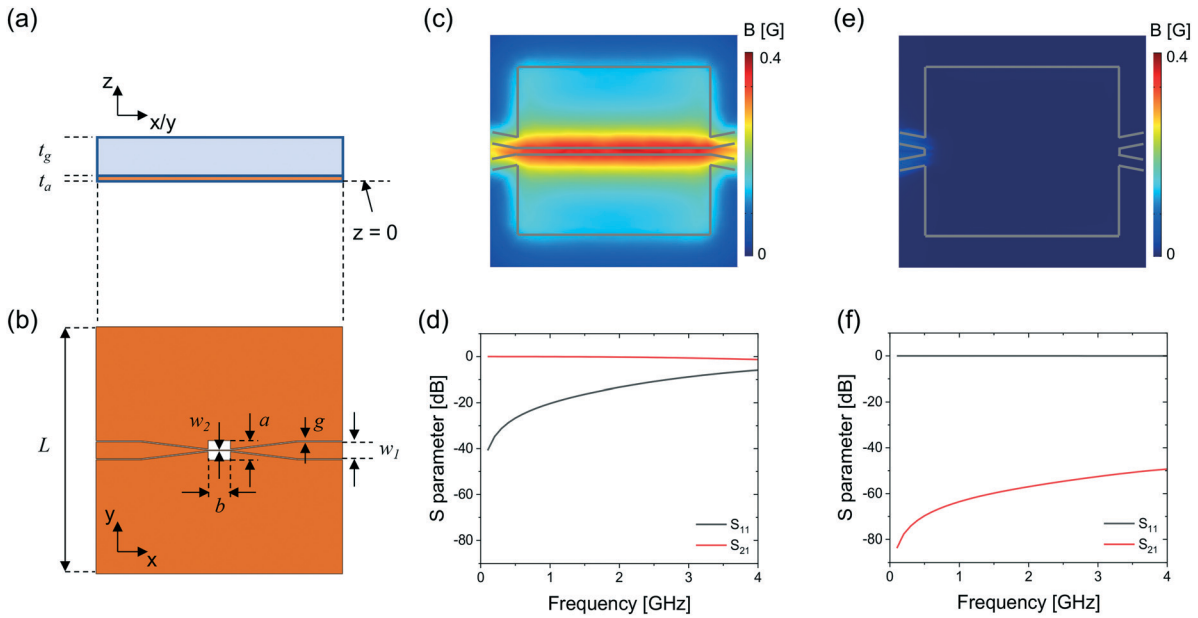

Fig. 2 Geometrical structure of the antenna coverslip in the (a) *xz* and (b) *xy* planes. The coverslip thickness is denoted as t_g, and t_a is that of the Au–Cr layer. *L* is the side length, and w_1 and w_2 are the widths of the transmission line at the coverslip edges and at the central thin wire, respectively. The notch height and width are *a* and *b*, respectively. In this particular case, *L* = 22 mm, w_1 = 1.5 mm, w_2 = 50 μm, *a* = 1.75 mm, *b* = 2.0 mm, t_g = 0.17 mm, and t_a = 100 nm. The Au–Cr layer is approximated as an infinitely thin PEC in the simulation (*i.e.*, $t_a \sim 0$ nm). (c) The computed spatial distribution of $|\boldsymbol{B}|$ at 2.87 GHz on the Au–Cr layer (*z* = 0 plane) and (d) corresponding simulated S_{11} (black) and S_{21} (red) spectra in the present notch-shaped coplanar waveguide structure. The $|\boldsymbol{B}|$ distribution and *S*-parameter spectra with the central thin-wire transmission line removed are shown in (e) and (f).

For more details on the notch-shaped antenna, we present parameter sweeps of the notch structures, that is, *a*, *b*, and w_2. As the notch size decreases (in terms of either *a* or *b*), the microwave transmission increases (a smaller S_{11} and larger S_{21}), as shown in Fig. S3(a)–(f).† The thin-wire width w_2 also affects the *S*-parameters: as w_2 increases, S_{11} (S_{21}) decreases (increases), as shown in Fig. S3(g)–(i).† We also analyzed the effect of the taper structures. As shown in Fig. S3(j)–(l),† the taper structure acts as an impedance transformer and improves S_{11} by ~5 dB and S_{21} by ~0.3 dB at 2.9 GHz.

3.2 Experimental characterization of the *S*-parameters

We next experimentally characterized the simulation results by measuring the *S*-parameters. Fig. 3(a) and (b) compare the simulated and experimental results measured by the vector network analyzer for S_{11} and S_{21}, respectively. For S_{11}, the reflection at 2.87 GHz is S_{11} = −8.13 dB (R = 15.4%) in the simulation and S_{11} = −11.0 dB (R = 7.94%) in the experiments. For S_{21}, the transmission is S_{21} = −0.726 dB (T = 84.6%) in the simulation and S_{21} = −6.32 dB (T = 23.4%) in the experiments. Here, R (the reflection microwave power) and T (the reflection transmission power) are converted from S_{11} and S_{21}, respectively, using eqn (1). In both spectra, the experimental results show one or two dips, as also observed in experiments on other antenna structures, including a simple coplanar antenna and omega-shaped thin-wire antennas (see Fig. S4†). At the junctions, we used 8 mm-long copper spring fingers (thickness 0.3 mm) to make electrical connections, as shown in Fig. 1(b). We associate these dips with a cavity resonance produced by impedance-mismatched reflections at the junctions between the coverslip antenna and the PCB. Indeed, these dips were found to disappear when an anisotropic conductive rubber connector was used instead of the spring fingers (see Fig. S5†). It is therefore likely that these dips arise from impedance mismatching at the junctions between the coverslip antenna and the PCB, and not from imperfections in the device fabrication.

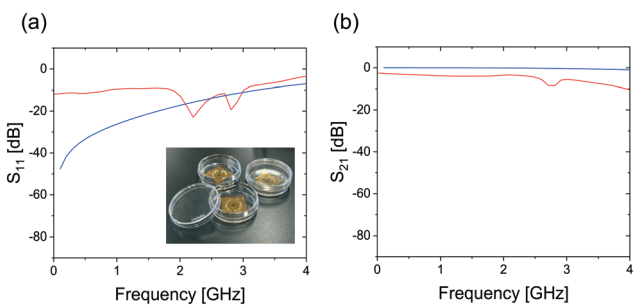

Fig. 3 *S*-parameter spectra of the fabricated devices for (a) S_{11} and (b) S_{21} (blue: simulation; red: experiment).

3.3 Experimental characterization of the magnetic field by ODMR measurements

Having designed the microwave circuit structure, we measured the ODMR for NDs spin-coated onto the antenna coverslips to experimentally confirm the simulations of the

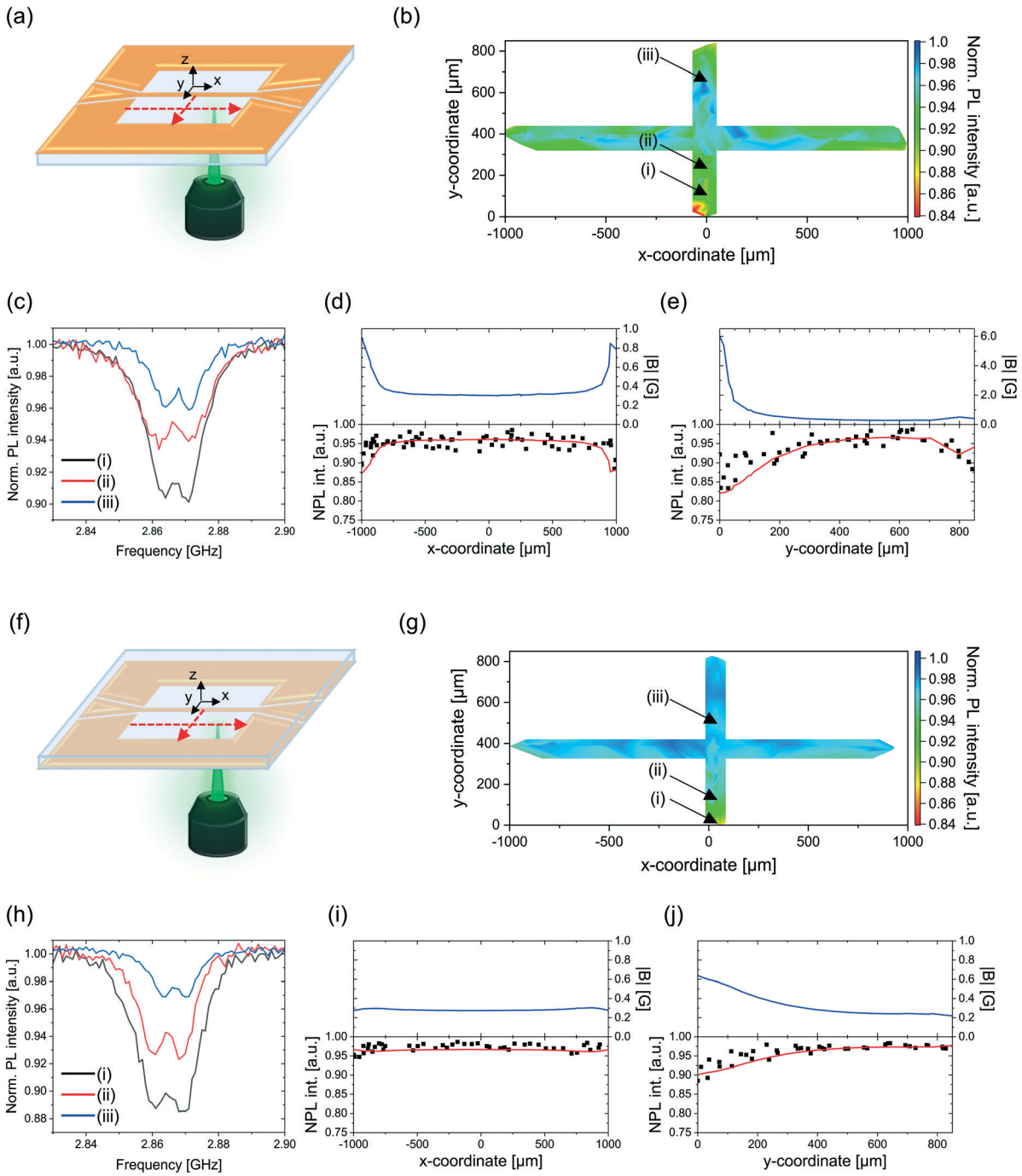

Fig. 4 (a) Schematic diagram for case 1, where NDs are deposited onto the Au–Cr layer side. (b) Heat map of experimental ODMR depth for case 1, and (c) the ODMR signals at positions (i)–(iii) in Fig. 4(b). (d) Dependence of the simulated $|\boldsymbol{B}|$ (top; blue line) and measured ODMR depth (bottom; black squares) with the simulated line calculated from the simulated $|\boldsymbol{B}|$ (bottom; red line) on the x- and (e) y-coordinates ("NPL int." stands for "Normalized PL intensity"). (f) Schematic diagram for case 2, where the antenna layer was located beneath the coverslip, while the NDs were spin-coated onto it. (g) Heat map of experimental ODMR depth for case 2, and (h) the ODMR signals at positions (i)–(iii) in Fig. 4(g) (i) dependence of $|\boldsymbol{B}|$ and ODMR depth on the x- and (j) y-coordinates. The normalized PL intensity ($\bar{I}$) is defined as $\bar{I} = I_{ON}/I_{OFF}$, where I_{ON} and I_{OFF} are the PL intensities when the microwave is on and off, respectively.

spatial distribution of $|\boldsymbol{B}|$. We measured the ODMR depth for two cases. In case 1, the NDs and antenna were situated on top of the coverslip (Fig. 4(a)), and we measured the ODMR along the line $x = -8.94$ μm and $y = 384$ μm. Fig. 4(b) shows the heat map of the experimental ODMR depth, and the positional dependence of its depth at positions (i)–(iii) is shown in Fig. 4(c). Fig. 4(d) and (e) show graphs of $|\boldsymbol{B}|$ calculated by the numerical simulation (top panels) and the corresponding plots of the ODMR depth as functions of x and y (bottom panels). In the bottom panels, the black

squares represent the experimental data and the red lines indicate the theoretical ODMR depth calculated from the simulated $|\boldsymbol{B}|$[66] (see ESI† for the details of the calculations). In case 2, the antenna layer was located beneath the coverslip, while the NDs were spin-coated onto it, that is, separated from the antenna by the coverslip thickness (Fig. 4(f)). We measured the ODMR along x = 31.3 μm and y = 389 μm like the measurements in case 1. Fig. 4(g) and (h) show the heat map of the experimental ODMR depth, and the positional dependence of its depth at positions (i)–(iii). Fig. 4(i) and (j) show the graphs of the simulated and experimental results, respectively. The experimental results of the ODMR depth closely matched the simulated ODMR depth in most regions.

To further confirm this comparison between the simulations and experiments in $|\boldsymbol{B}|$,[67] we measured Rabi nutations for NDs located close to the central thin-wire transmission line. Fig. 5(a) and (b) show a representative Rabi nutation and its square-root microwave power dependence for an ND located at (x, y). We obtained the Rabi nutation frequencies (f_R) by fitting the data to the theoretical equation,[68,69] giving f_R = 4.5 MHz for this particular ND with 63 mW microwave power (see ESI† for the detailed estimation of microwave input power) and obtained a mean of f_R = 4.4 ± 0.8 MHz for four NDs measured near the transmission wire (they were located 25–57 μm from the transmission line). This Rabi nutation frequency corresponds to $|\boldsymbol{B}|$ = 2.2 ± 0.41 G based on the following equation:[70–72]

$$f_R = \frac{\gamma|\boldsymbol{B}|}{\sqrt{2}}, \quad (2)$$

where γ = 2.8 MHz G^{-1} is the NV gyromagnetic ratio. This value is consistent with the numerical simulation in the corresponding region ($|\boldsymbol{B}| \approx$ 2.5 G). Note that eqn (2) assumes that B is perpendicular to the NV axes, which may cause an uncertainty in estimating $|\boldsymbol{B}|$ (see ESI†).

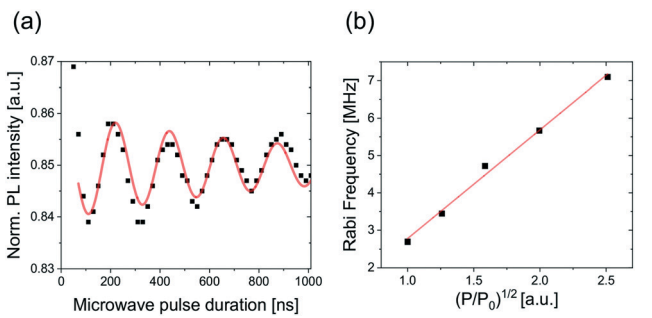

Fig. 5 (a) Representative Rabi nutation profile of NDs deposited close to the central thin wire. (black dots: experiment; red line: fitting based on the theoretical sine-damping equation). (b) Rabi nutation frequency as a function of the normalized microwave power ($(P/P_0)^{1/2}$), where P and P_0 are the input microwave power and the minimum ODMR observable input microwave power, respectively (black dots: experiment; red line: linear fit).

3.4 Biological application: cultured cells

We used the notch-shaped coplanar waveguide chip devices to perform ODMR measurements of NDs in cultured cells. We glued the glass face of the devices (not the Au–Cr face) onto 35 mm plastic dishes and seeded the cells in the dishes. Fig. 6(a) shows the flow diagram of ODMR measurement preparation using cells. The glass face of the chip device was coated with collagen to improve the cell adhesion before seeding. We then introduced carboxylated NDs into HeLa cells by endocytosis, as previously described.[55,73] Fig. 6(b) shows a low-magnification bright-field image of HeLa cells in the chip devices. Fig. 6(c) merges a bright-field image with red fluorescence acquired in our home-built microscope. We measured the ODMR of an isolated ND, indicated by a yellow arrow, and successfully obtained the ODMR spectrum, as shown in Fig. 6(d). Comparable ODMR depths can be observed for NDs in other cells distributed in the center of the notch area (see Fig. S7(c)†). For a mean depth of 0.951, we estimated $|\boldsymbol{B}|$ = 0.35 ± 0.01 G using eqn (S3†) and its error propagation, which reflects the uniformity of $|\boldsymbol{B}|$ in the notch area. The estimation uncertainty of 0.01 G was comparable to that obtained for NDs on coverslip in the central notch region (from x = −600 μm to +600 μm in Fig. 4(i)).

3.5 Biological application: tadpole tissue

Our devices provide an observation area (1.75 × 2.0 mm^2 square) that is sufficiently large for various tissue experiments, beyond the reach of previous waveguide-based antennas. As a demonstration, we used tail tissue from *Xenopus laevis* tadpoles. *Xenopus* is a common animal model used in developmental biology[74–76] for studying regeneration and inflammation.[77–80] For example, microscopy studies have observed the dynamics of regeneration, degeneration, and metamorphosis in amputated tail tissue.[81–85] Therefore, we amputated tail fragments from stage-54 *Xenopus* tadpoles whose tails were labeled with PG-NDs by intramuscular injection with syringes before the final stage of tail degeneration (stage 66).[86] The fragments were placed on dish-type chip devices and subjected to ODMR detection, as shown in Fig. 6(e). Fig. 6(f) shows a merged bright-field and red-fluorescence image of the tissue fragments. The low background red-wavelength fluorescence enabled the observation of multiple ND fluorescence spots in the tail tissue. In contrast to the cell experiments described above, the NDs in the tissue underwent noticeable Brownian motion, which disturbed the stable ODMR measurements. Therefore, we reduced the ODMR measurement time by decreasing the sampling frequency and successfully acquired the ODMR spectra of NDs in the tissue, as shown in Fig. 6(g). The ODMR depth was 0.936 and the NDs in the other tissue (Fig. S7(f)†) also showed ODMR depths within the variation comparable to the coverslip case (Fig. 4).

3.6 Biological application: nematode worms *in vivo*

Exploiting the large observation area provided by our devices, we performed ODMR measurements over the entire body of

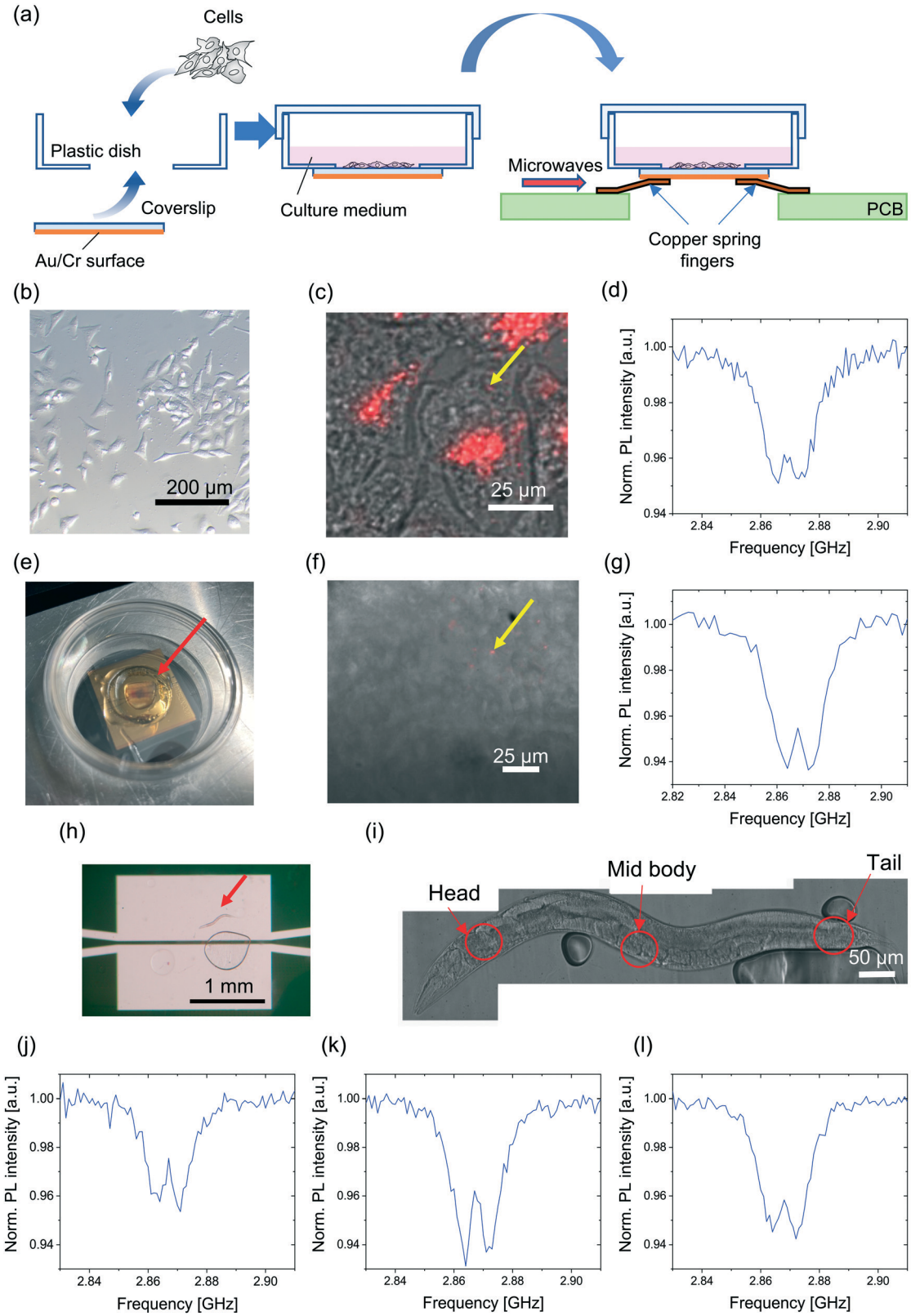

Fig. 6 (a) Flow diagram of the device assembly and ODMR measurements using cells. (b) Bright-field image of living HeLa cells with a low magnification objective. (c) Merged bright-field image with red fluorescence of ND-labeled HeLa cells acquired using the ODMR microscope. (d) ODMR spectrum of the ND, indicated by the yellow arrow in Fig. 6(c). (e) Photograph of a piece of tissue fragment of a stage-54 *Xenopus* tadpole tail in the dish-type chip devices. (f) Merged bright-field image with red fluorescence of the ND-injected tissue acquired using the ODMR microscope and (g) ODMR spectrum of the ND indicated by the yellow arrow in Fig. 6(f). (h) Microscopic photo of *C. elegans* in the notch area of the chip devices. An air bubble was included below the worm. (i) Microscopic photomontage of another worm in the notch area, indicating the body parts measured for ODMR. (j)–(l) Representative ODMR spectra of NDs found in three body parts: head, middle body, and tail, respectively.

C. elegans in vivo. We microinjected PG-NDs into the gonads of *C. elegans*, as previously reported.[20,59] After a 24 h recovery, we placed a worm on the agar pads for anesthetization and transferred the entire pad to the notch area of the device. Fig. 6(h) shows a microscope photograph of the *C. elegans* immobilized in the notch area. The worm was oriented parallel to the transmission line as much as possible to ensure uniform excitation of the magnetic field along the worm axis. We then measured the ODMR spectra of representative NDs located in the following three body parts (neck, midbody, and tail), as shown in Fig. 6(i). The observed ODMR depths have variations of 0.963, 0.942, and 0.953 for Fig. 6(j)–(l). This variation is consistent with the intrinsic variation observed for NDs directly deposited on the glass surface of the devices (see Fig. 3), which confirms the uniformity of the magnetic field intensity over the entire worm body. The uniform ODMR depths in the central notch region were confirmed in different worms, as illustrated in Fig. S7(i).†

4 Discussion

This study presents a glass-patternable notch-shaped coplanar waveguide microwave antenna that provides a millimeter-scale observation area and a gigahertz frequency bandwidth for performing ODMR measurements on diamond NV centers in biological samples. Conventional antennas used in biological ODMR experiments involving NDs include thin wires, coils, and omega-shaped antennas.[8,40,43,45,46,56] Thin-wire antennas have been widely used with samples such as cells and worms because of their simple fabrication and wide frequency bandwidth. However, they display strong microwave reflection up to $S_{11} \sim -3$ dB and have a limited irradiation area at a distance of ~100 μm from the wire.[56] Coils have been frequently used in biological ODMR experiments to provide microwave radiation to nearby samples. Fig. S8(a)–(c)† show the microwave irradiation characteristics of conventional coils. Coil miniaturization is a significant technical challenge. Because the ODMR of NV centers is usually performed in the *S*-band (2–4 GHz), impedance matching to 50 Ω coaxial cables requires approximately 1 mm in diameter, resulting in low $|\boldsymbol{B}|$ intensity (see Fig. S8(b)†). This difficulty of balancing the trade-off between the impedance matching and high $|\boldsymbol{B}|$ intensity may hinder compatibility with the measurement systems. Accurate prediction of the ODMR signal intensity is also challenging because the distance between the NDs and coils cannot be defined with 10 μm resolution. Omega-shaped antennas have become an appealing alternative for biological ODMR applications. These antennas are of two types: impedance-matched fully resonant omega shapes[8] and non-resonant omega shapes.[45] Impedance-matched omega-shapes have been recently employed for portable ODMR detection systems because of their high input efficiency and millimeter-scale spatial uniformity of $|\boldsymbol{B}|$.[8] Conversely, their frequency response shows resonance, which is undesirable for broad-bandwidth applications such as vector magnetometry that reads multiple ODMR dips from four NV axes spanning over 200 MHz width.[47–50,87] We compare the microwave characteristics of a representative non-resonant omega shape and the present notch-shaped coplanar antenna in Fig. S8(d)–(f).† The non-resonant omega shape provides a uniform $|\boldsymbol{B}|$ over a length scale on the order of 10 μm by perturbing the steep $|\boldsymbol{B}|$ distribution around the thin wire line. It also affords a broad bandwidth that is comparable to the coplanar waveguides. Alternatively, the effect of the omega shape appears within 100 μm, and becomes insignificant in the opposite-plane configuration (case 2 in Fig. 4), where the NDs are separated from the Au–Cr layer by 0.17 mm across the coverslip, approaching the same microwave characteristics as the present notch-shaped coplanar structure. In practice, the size of the omega shape has an upper limit of 500 μm.

In addition to the large detection area and broad bandwidth, the notch-shaped coplanar structure is biocompatible and scalable. For biocompatibility, by bringing the Au–Cr layer to the bottom side of the coverslip, the device can be used in exactly the same way as a conventional glass-bottom dish. The plain glass surface inside the dish-style device allows various surface coatings for culturing cells and tissue. Indeed, we confirmed that adipose-tissue-derived stem cells,[56] which are more delicate than HeLa cells, can be successfully cultured on our collagen-coated devices (see Fig. S9†). The concept of docking the devices onto a PCB for making circuit connections also helps to conserve the sample quality by shortening the handling time. For the scalability, the flat *S*-parameter spectral profiles enable the integration of multiple observation areas (triple wells in this example) within 15 mm on a single chip without incurring a significant deterioration of the microwave characteristics, as shown in Fig. S5.† Such scalability is not easily attainable with S-band microwave circuits because of the size limitation originating from the centimeter-long wavelength in this band (3 GHz corresponds to 10 cm wavelength and its quarter is 2.5 cm). It is anticipated that such triple-well chip devices can be readily extended to large-scale multi-well plates for plate reading in ODMR-based assays.

5 Conclusion

Quantum nano-sensors involving fluorescent NDs are a promising new technology for multimodal bioassays that are particularly well suited to on-chip device miniaturization. However, the miniaturization of microwave excitation circuits used with optical detection is challenging because they operate at centimeter wavelengths. To address this issue, we developed a method to quantitatively predict the ODMR signal intensity by employing the FEM-based numerical simulations and proposed a notch-shaped coplanar antenna on a glass coverslip that can be assembled into various bioassay platforms, including dishes, microscope slides, and multi-well plates. This notch-shaped structure provided a

millimeter-scale ODMR detection area over 1.5 × 2.0 mm^2 and broadband low-reflection characteristics of microwaves ($R \approx 8\%$ over a few gigahertz). This device achieved uniform ODMR detection within cells, tadpole tail tissue, and *C. elegans*. The concept of this notch-shaped coplanar antenna and methodology for the quantitative modeling of ODMR characteristics will facilitate the integration of diamond-based quantum sensing technology into chip-based bioassays.

Author contributions

K. O. and M. F. designed the research. K. O. performed the numerical simulation. K. O., Y. N., M. Tnk., and E. S. performed the device fabrication. L. Z., Y. Z. and N. K. synthesized the PG-NDs. K. O., Y. N., T. M., S. M., M. Tkng., H. Y., and Y. B. performed the cell experiments. Y. T., Y. Z., Y. I. and E. K.-N. prepared the worms and their ND labeling. K. O., K. Y. and Y. I. performed the tadpole experiments. K. O., Y. N., Y. I., Y. T., and M. F. performed the ODMR experiments and analyses. All the authors participated in the discussion and writing of the paper.

Conflicts of interest

There are no conflicts to declare.

Acknowledgements

We thank S. Sakakihara, Y. Umehara, and Y. Shikano for their support in the device fabrication, bio-sample preparation and discussion, respectively. A part of this work was supported by the "Nanotechnology Platform Project (Nanotechnology Open Facilities in Osaka University) of MEXT (JPMXP09F21OS0055). We acknowledge funding from JSPS-KAKENHI (19K21935, 20H00335, 20KK0317), AMED (JP21zf0127004), JST (JPMJMI21G1), the MEXT-LEADER program, the Mazda Foundation, and Osaka City University Strategic Research Grant 2017–2020, MEXT Quantum Leap Flagship Program (MEXT Q-LEAP, JPMXS0120330644).

References

1 H. T. Ngo, H.-N. Wang, A. M. Fales, B. P. Nicholson, C. W. Woods and T. Vo-Dinh, *Analyst*, 2014, **139**, 5655–5659.
2 H. Tani, K. Maehana and T. Kamidate, *Anal. Chem.*, 2004, **76**, 6693–6697.
3 M. Rothbauer, H. Zirath and P. Ertl, *Lab Chip*, 2018, **18**, 249–270.
4 G. A. Ferrier, S. F. Romanuik, D. J. Thomson, G. E. Bridges and M. R. Freeman, *Lab Chip*, 2009, **9**, 3406–3412.
5 F. C. Ziem, N. S. Götz, A. Zappe, S. Steinert and J. Wrachtrup, *Nano Lett.*, 2013, **13**, 4093–4098.
6 J. Wackerlig and R. Schirhagl, *Anal. Chem.*, 2016, **88**, 250–261.
7 T. Rendler, J. Neburkova, O. Zemek, J. Kotek, A. Zappe, Z. Chu, P. Cigler and J. Wrachtrup, *Nat. Commun.*, 2017, **8**, 1–9.
8 B. S. Miller, L. Bezinge, H. D. Gliddon, D. Huang, G. Dold, E. R. Gray, J. Heaney, P. J. Dobson, E. Nastouli and J. J. Morton, *et al.*, *Nature*, 2020, **587**, 588–593.
9 S. Haziza, N. Mohan, Y. Loe-Mie, A.-M. Lepagnol-Bestel, S. Massou, M.-P. Adam, X. L. Le, J. Viard, C. Plancon and R. Daudin, *et al.*, *Nat. Nanotechnol.*, 2017, **12**, 322–328.
10 G. Kucsko, P. C. Maurer, N. Y. Yao, M. Kubo, H. J. Noh, P. K. Lo, H. Park and M. D. Lukin, *Nature*, 2013, **500**, 54–58.
11 D. A. Simpson, E. Morrisroe, J. M. McCoey, A. H. Lombard, D. C. Mendis, F. Treussart, L. T. Hall, S. Petrou and L. C. Hollenberg, *ACS Nano*, 2017, **11**, 12077–12086.
12 L. Toraille, K. Aïzel, É. Balloul, C. Vicario, C. Monzel, M. Coppey, E. Secret, J.-M. Siaugue, J. Sampaio and S. Rohart, *et al.*, *Nano Lett.*, 2018, **18**, 7635–7641.
13 S. Claveau, J.-R. Bertrand and F. Treussart, *Micromachines*, 2018, **9**, 247.
14 L. Nie, A. Nusantara, V. Damle, R. Sharmin, E. Evans, S. Hemelaar, K. van der Laan, R. Li, F. P. Martinez and T. Vedelaar, *et al.*, *Sci. Adv.*, 2021, **7**, eabf0573.
15 H. C. Davis, P. Ramesh, A. Bhatnagar, A. Lee-Gosselin, J. F. Barry, D. R. Glenn, R. L. Walsworth and M. G. Shapiro, *Nat. Commun.*, 2018, **9**, 1–9.
16 K. J. van der Laan, A. Morita, F. P. Perona-Martinez and R. Schirhagl, *Nanomaterials*, 2020, **10**, 372.
17 M. Fujiwara, S. Sun, A. Dohms, Y. Nishimura, K. Suto, Y. Takezawa, K. Oshimi, L. Zhao, N. Sadzak and Y. Umehara, *et al.*, *Sci. Adv.*, 2020, **6**, eaba9636.
18 Y. Zhu, J. Li, W. Li, Y. Zhang, X. Yang, N. Chen, Y. Sun, Y. Zhao, C. Fan and Q. Huang, *Theranostics*, 2012, **2**, 302.
19 A. Krueger, *Chem. – Eur. J.*, 2008, **14**, 1382–1390.
20 N. Mohan, C.-S. Chen, H.-H. Hsieh, Y.-C. Wu and H.-C. Chang, *Nano Lett.*, 2010, **10**, 3692–3699.
21 S. R. Hemelaar, K. J. van der Laan, S. R. Hinterding, M. V. Koot, E. Ellermann, F. P. Perona-Martinez, D. Roig, S. Hommelet, D. Novarina and H. Takahashi, *et al.*, *Sci. Rep.*, 2017, **7**, 1–7.
22 S. Sotoma, F.-J. Hsieh, Y.-W. Chen, P.-C. Tsai and H.-C. Chang, *Chem. Commun.*, 2018, **54**, 1000–1003.
23 G. Reina, L. Zhao, A. Bianco and N. Komatsu, *Angew. Chem., Int. Ed.*, 2019, **58**, 17918–17929.
24 L. Rondin, J.-P. Tetienne, T. Hingant, J.-F. Roch, P. Maletinsky and V. Jacques, *Rep. Prog. Phys.*, 2014, **77**, 056503.
25 D. Maclaurin, L. Hall, A. Martin and L. Hollenberg, *New J. Phys.*, 2013, **15**, 013041.
26 V. R. Horowitz, B. J. Alemán, D. J. Christle, A. N. Cleland and D. D. Awschalom, *Proc. Natl. Acad. Sci. U. S. A.*, 2012, **109**, 13493–13497.
27 F. Dolde, H. Fedder, M. W. Doherty, T. Nöbauer, F. Rempp, G. Balasubramanian, T. Wolf, F. Reinhard, L. C. Hollenberg and F. Jelezko, *et al.*, *Nat. Phys.*, 2011, **7**, 459–463.
28 T. Iwasaki, W. Naruki, K. Tahara, T. Makino, H. Kato, M. Ogura, D. Takeuchi, S. Yamasaki and M. Hatano, *ACS Nano*, 2017, **11**, 1238–1245.
29 K. Bian, W. Zheng, X. Zeng, X. Chen, R. Stöhr, A. Denisenko, S. Yang, J. Wrachtrup and Y. Jiang, *Nat. Commun.*, 2021, **12**, 2457.

30 P. Neumann, I. Jakobi, F. Dolde, C. Burk, R. Reuter, G. Waldherr, J. Honert, T. Wolf, A. Brunner and J. H. Shim, *et al.*, *Nano Lett.*, 2013, **13**, 2738–2742.
31 M. Fujiwara and Y. Shikano, *Nanotechnology*, 2021, **32**, 482002.
32 N. Wang, G.-Q. Liu, W.-H. Leong, H. Zeng, X. Feng, S.-H. Li, F. Dolde, H. Fedder, J. Wrachtrup and X.-D. Cui, *et al.*, *Phys. Rev. X*, 2018, **8**, 011042.
33 R. Mazurczyk, J. Vieillard, A. Bouchard, B. Hannes and S. Krawczyk, *Sens. Actuators, B*, 2006, **118**, 11–19.
34 S. Dochow, M. Becker, R. Spittel, C. Beleites, S. Stanca, I. Latka, K. Schuster, J. Kobelke, S. Unger and T. Henkel, *et al.*, *Lab Chip*, 2013, **13**, 1109–1113.
35 J. Qi, B. Li, X. Wang, L. Fu, L. Luo and L. Chen, *Anal. Chem.*, 2018, **90**, 11827–11834.
36 D. J. Marchiarullo, A. H. Sklavounos, K. Oh, B. L. Poe, N. S. Barker and J. P. Landers, *Lab Chip*, 2013, **13**, 3417–3425.
37 G. Yesiloz, M. S. Boybay and C. L. Ren, *Lab Chip*, 2015, **15**, 4008–4019.
38 D. Wong, G. Yesiloz, M. S. Boybay and C. L. Ren, *Lab Chip*, 2016, **16**, 2192–2197.
39 Y. Chen, S. F. Hung, W. K. Lo, Y. Chen, Y. Shen, K. Kafenda, J. Su, K. Xia and S. Yang, *Nat. Commun.*, 2020, **11**, 1–8.
40 K. Fukushige, H. Kawaguchi, K. Shimazaki, T. Tashima, H. Takashima and S. Takeuchi, *Appl. Phys. Lett.*, 2020, **116**, 264002.
41 N. Sadzak, M. Héritier and O. Benson, *Sci. Rep.*, 2018, **8**, 1–8.
42 W. Jia, Z. Shi, X. Qin, X. Rong and J. Du, *Rev. Sci. Instrum.*, 2018, **89**, 064705.
43 R. Igarashi, Y. Yoshinari, H. Yokota, T. Sugi, F. Sugihara, K. Ikeda, H. Sumiya, S. Tsuji, I. Mori and H. Tochio, *et al.*, *Nano Lett.*, 2012, **12**, 5726–5732.
44 A. Ajoy, R. Nazaryan, E. Druga, K. Liu, A. Aguilar, B. Han, M. Gierth, J. T. Oon, B. Safvati and R. Tsang, *et al.*, *Rev. Sci. Instrum.*, 2020, **91**, 023106.
45 J. Choi, H. Zhou, R. Landig, H.-Y. Wu, X. Yu, S. E. Von Stetina, G. Kucsko, S. E. Mango, D. J. Needleman and A. D. Samuel, *et al.*, *Proc. Natl. Acad. Sci. U. S. A.*, 2020, **117**, 14636–14641.
46 S. V. Bolshedvorskii, V. V. Vorobyov, V. V. Soshenko, V. A. Shershulin, J. Javadzade, A. I. Zeleneev, S. A. Komrakova, V. N. Sorokin, P. I. Belobrov and A. N. Smolyaninov, *et al.*, *Opt. Mater. Express*, 2017, **7**, 4038–4049.
47 J. M. Schloss, J. F. Barry, M. J. Turner and R. L. Walsworth, *Phys. Rev. Appl.*, 2018, **10**, 034044.
48 H. Clevenson, L. M. Pham, C. Teale, K. Johnson, D. Englund and D. Braje, *Appl. Phys. Lett.*, 2018, **112**, 252406.
49 R. Igarashi, T. Sugi, S. Sotoma, T. Genjo, Y. Kumiya, E. Walinda, H. Ueno, K. Ikeda, H. Sumiya, H. Tochio, Y. Yoshinari, Y. Harada and M. Shirakawa, *J. Am. Chem. Soc.*, 2020, **142**, 7542–7554.
50 M. Tsukamoto, K. Ogawa, H. Ozawa, T. Iwasaki, M. Hatano, K. Sasaki and K. Kobayashi, *Appl. Phys. Lett.*, 2021, **118**, 264002.
51 S. J. DeVience, L. M. Pham, I. Lovchinsky, A. O. Sushkov, N. Bar-Gill, C. Belthangady, F. Casola, M. Corbett, H. Zhang and M. Lukin, *et al.*, *Nat. Nanotechnol.*, 2015, **10**, 129–134.
52 J. Smits, J. T. Damron, P. Kehayias, A. F. McDowell, N. Mosavian, I. Fescenko, N. Ristoff, A. Laraoui, A. Jarmola and V. M. Acosta, *Sci. Adv.*, 2019, **5**, eaaw7895.
53 J. Holzgrafe, Q. Gu, J. Beitner, D. M. Kara, H. S. Knowles and M. Atatüre, *Phys. Rev. Appl.*, 2020, **13**, 044004.
54 D. M. Pozar, *Microwave Engineering*, John wiley & sons, 3rd edn, 2005.
55 Y. Nishimura, K. Oshimi, Y. Umehara, Y. Kumon, K. Miyaji, H. Yukawa, Y. Shikano, T. Matsubara, M. Fujiwara and Y. Baba, *et al.*, *Sci. Rep.*, 2021, **11**, 1–12.
56 H. Yukawa, M. Fujiwara, K. Kobayashi, Y. Kumon, K. Miyaji, Y. Nishimura, K. Oshimi, Y. Umehara, Y. Teki and T. Iwasaki, *et al.*, *Nanoscale Adv.*, 2020, **2**, 1859–1868.
57 Y. Izutsu, *Cold Spring Harb. Protoc.*, 2019, **2019**, pdb–prot099788.
58 Y. Izutsu and M. Maéno, *Methods Mol. Med.*, 2005, 149–158.
59 L. Zhao, T. Takimoto, M. Ito, N. Kitagawa, T. Kimura and N. Komatsu, *Angew. Chem., Int. Ed.*, 2011, **50**, 1388–1392.
60 S. Brenner, *Genetics*, 1974, **77**, 71–94.
61 R. Tsukahara, M. Fujiwara, Y. Sera, Y. Nishimura, Y. Sugai, C. Jentgens, Y. Teki, H. Hashimoto and S. Shikata, *ACS Appl. Nano Mater.*, 2019, **2**, 3701–3710.
62 M. Fujiwara, A. Dohms, K. Suto, Y. Nishimura, K. Oshimi, Y. Teki, K. Cai, O. Benson and Y. Shikano, *Phys. Rev. Res.*, 2020, **2**, 043415.
63 M. Fujiwara, R. Tsukahara, Y. Sera, H. Yukawa, Y. Baba, S. Shikata and H. Hashimoto, *RSC Adv.*, 2019, **9**, 12606–12614.
64 R. Sefa and A. Maraj, *Proceedings of the 10th WSEAS international conference on Telecommunications and informatics and microelectronics, nanoelectronics, optoelectronics, and WSEAS international conference on Signal processing*, Canary Islands, Spain, 2011, pp. 27–29.
65 J. M. Pérez-Escudero, A. E. Torres-García, R. Gonzalo and I. Ederra, *Electronics*, 2018, **7**, 215.
66 A. Dréau, M. Lesik, L. Rondin, P. Spinicelli, O. Arcizet, J.-F. Roch and V. Jacques, *Phys. Rev. B: Condens. Matter Mater. Phys.*, 2011, **84**, 195204.
67 K. Bayat, J. Choy, M. F. Baroughi, S. Meesala and M. Loncar, *Nano Lett.*, 2014, **14**, 1208–1213.
68 J. C. Camparo and R. P. Frueholz, *Phys. Rev. A: At., Mol., Opt. Phys.*, 1988, **38**, 6143.
69 S. Bertaina, C.-E. Dutoit, J. Van Tol, M. Dressel, B. Barbara and A. Stepanov, *Phys. Rev. B: Condens. Matter Mater. Phys.*, 2014, **90**, 060404.
70 R. Hanson, V. Dobrovitski, A. Feiguin, O. Gywat and D. Awschalom, *Science*, 2008, **320**, 352–355.
71 K. Sasaki, Y. Monnai, S. Saijo, R. Fujita, H. Watanabe, J. Ishi-Hayase, K. M. Itoh and E. Abe, *Rev. Sci. Instrum.*, 2016, **87**, 053904.
72 H. H. Vallabhapurapu, J. P. Slack-Smith, V. K. Sewani, C. Adambukulam, A. Morello, J. J. Pla and A. Laucht, *Phys. Rev. Appl.*, 2021, **16**, 044051.
73 J. Slegerova, I. Rehor, J. Havlik, H. Raabova, E. Muchova and P. Cigler, *Intracellular delivery II*, Springer, 2014, pp. 363–401.
74 A. K. Sater and S. A. Moody, *Genesis*, 2017, **55**, e22997.

75 H. Straka and J. Simmers, *Dev. Neurobiol.*, 2012, **72**, 649–663.
76 Y. Nakai, K. Nakajima and Y. Yaoita, *Biomol. Concepts*, 2017, **8**, 179–183.
77 J. Slack, G. Lin and Y. Chen, *Cell. Mol. Life Sci.*, 2008, **65**, 54–63.
78 L. S. Phipps, L. Marshall, K. Dorey and E. Amaya, *Development*, 2020, **147**, dev180844.
79 M. W. King, A. W. Neff and A. L. Mescher, *Anat. Rec.*, 2012, **295**, 1552–1561.
80 H. Davaapil, J. P. Brockes and M. H. Yun, *Development*, 2017, **144**, 106–114.
81 R. Weber, *Gen. Comp. Endocrinol.*, 1969, **2**, 408–416.
82 K. Niki, H. Namiki, S. Kikuyama and K. Yoshizato, *Dev. Biol.*, 1982, **94**, 116–120.
83 Y. Izutsu, K. Yoshizato and S. Tochinai, *Differentiation*, 1996, **60**, 277–286.
84 K. Nakajima, I. Tazawa and Y.-B. Shi, *Gen. Comp. Endocrinol.*, 2019, **277**, 66–72.
85 H. Tsujioka, T. Kunieda, Y. Katou, K. Shirahige, T. Fukazawa and T. Kubo, *Nat. Commun.*, 2017, **8**, 1–12.
86 K. Mukaigasa, A. Hanasaki, M. Maéno, H. Fujii, S.-I. Hayashida, M. Itoh, M. Kobayashi, S. Tochinai, M. Hatta and K. Iwabuchi, *et al.*, *Proc. Natl. Acad. Sci. U. S. A.*, 2009, **106**, 18309–18314.
87 D. Le Sage, K. Arai, D. R. Glenn, S. J. DeVience, L. M. Pham, L. Rahn-Lee, M. D. Lukin, A. Yacoby, A. Komeili and R. L. Walsworth, *Nature*, 2013, **496**, 486–489.